RESEARCH PAPER

Application of astigmatism µ-PTV to analyze the vortex structure of AC electroosmotic flows

Zhipeng Liu · Michel F. M. Speetjens ·
Arjan J. H. Frijns · Anton A. van Steenhoven

Abstract The three-dimensional (3D) flow due to AC electroosmotic (ACEO) forcing on an array of interdigitated symmetric electrodes in micro-channels is experimentally analyzed using astigmatism micro-particle tracking velocimetry (astigmatism µ-PTV). Upon application of the AC electric field with a frequency of 1,000 Hz and a voltage of 2 Volts peak–peak, the obtained 3D particle trajectories exhibit a vortical structure of ACEO flow above the electrodes. Two alternating time delays (0.03 and 0.37 s) were used to measure the flow field with a wide range of velocities, including error analysis. Presence and properties of the vortical flow were quantified. The steady nature and the quasi-2D character of the vortices can combine the results from a series of measurements into one dense data set. This facilitates accurate evaluation of the velocity field by data-processing methods. The primary circulation of the vortices due to ACEO forcing is given in terms of the spanwise component of vorticity. The outline of the vortex boundary is determined via the eigenvalues of the strain-rate tensor. Overall, astigmatism µ-PTV is proven to be a reliable tool for quantitative analysis of ACEO flow.

Keywords AC electroosmosis · 3D velocity measurement · Vortical flow · Microfluidics

Z. Liu (✉) · M. F. M. Speetjens · A. J. H. Frijns ·
A. A. van Steenhoven
Mechanical Engineering Department, Eindhoven University
of Technology, P.O.Box 513, 5600 MB Eindhoven,
The Netherlands
e-mail: zh.liu@tue.nl

1 Introduction

AC electroosmosis (ACEO) is increasingly utilized in micro/nano-fluidic applications due to its ability to generate a flow using a low-voltage AC electric field (Ramos et al. 1999). The low voltages admitted by ACEO offer essential advantages over the conventional DC electroosmosis systems relying on high voltages. Namely, undesirable side effects, e.g., bubble formation due to electrolysis and electrolyte contamination due to Faradaic reactions, are significantly weaker or absent altogether in ACEO. ACEO as a flow-forcing technique has a great potential for the actuation and manipulation of micro-flows and has found successful applications in micro-pumping (Brown et al. 2000; Studer et al. 2004; Bazant and Ben 2006), micromixing (Sasaki et al. 2006; Huang et al. 2007), and manipulation of polarizable particles (Gagnon and Chang 2005; Wu et al. 2005; Park and Beskok 2008).

In order to obtain a complete understanding of ACEO-induced flow, flow visualization is the main approach employed. By tracing individual seeding particles, Ramos et al. (1998) first reported a local flow field parallel with the electrode surfaces using a low amplitude AC signal in aqueous electrolyte, which exhibited the fundamental description of the ACEO flow. Later, based on the pathlines of tracer particles, Green et al. (2002) qualitatively demonstrated the vortical structure of an ACEO flow above a pair of symmetric electrodes. So far, AC electroosmotic flow has been observed experimentally on various electrode surfaces (Bazant and Ben 2006; Huang et al. 2007; Garacia-Sanchez et al. 2006; Kim et al. 2009; Green et al. 2000; Motosuke et al. 2013). However, the experimental descriptions of the ACEO flow are mainly restricted to a two-dimensional (2D) flow field, even though the ACEO flow shows a three-dimensional flow structure. Therefore,

in-depth experimental investigations on the 3D velocity field of ACEO flow are of great importance to further understand ACEO-induced flow.

Recently, an astigmatism micro-particle tracking velocimetry (astigmatism μ-PTV) was developed (Chen and Angarita-Jaimes 2009; Cierpka et al. 2010a). Compared to standard μ-PIV/PTV techniques which give a 2-dimensional and 2-component velocity distribution, astigmatism μ-PTV technique offers a 3-dimensional and 3-component full volume measurement of the velocity field (Cierpka et al. 2010a, b). By using the full numerical aperture of one microscope objective, astigmatism μ-PTV technique has a large range of the measurable depth, without any limitation by the optical access as tomographic μ-PIV and stereo μ-PIV systems do (Cierpka et al. 2011). This technique has been successfully used to measure a 3D velocity field of the electrothermal micro-vortex on a parallel-plate electrode surface (Kumar et al. 2010).

In the present study, the 3D flow structure of ACEO flow is experimentally investigated using an astigmatism μ-PTV technique. In contrast to previous experiments using a single coplanar electrode pair (Green et al. 2000), this study employs an array of interdigitated symmetric electrodes; this is a very common electrokinetic geometry in micro-flow systems. As the velocity field is expected to vary in a broad range, two different time delays (0.03 and 0.37 s) are used, for which the uncertainty of the velocity measurement is estimated. Finally, the strength of ACEO vortex is investigated in terms of spanwise component of vorticity and circulation.

2 Problem definition

The flow domain consists of a straight rectangular channel, shown schematically in Fig. 1. An array of interdigitated symmetric electrodes is aligned on the bottom of the channel. The electrodes are spatially periodic, and each period is of horizontal extent $L = W + G$, with W and G the electrode and gap widths, respectively. Assuming the effects of the channel side walls are negligible, the theory predicts that the symmetry of the electrodes should result in two symmetrical counter-rotating vortices above each electrode (Ramos et al. 2003; Speetjens et al. 2011). In the present work, the vortex structure in this device is studied experimentally.

Based on the velocity field $\mathbf{u} = (u_x, u_y, u_z)$, the ACEO-induced vortex is described in terms of the spanwise component of the vorticity ω_y

$$\omega_y = \frac{\partial u_x}{\partial z} - \frac{\partial u_z}{\partial x}, \qquad (1)$$

where x, y, and z are three components of the coordinate system as shown in Fig. 1. The circulation, i.e., strength, of
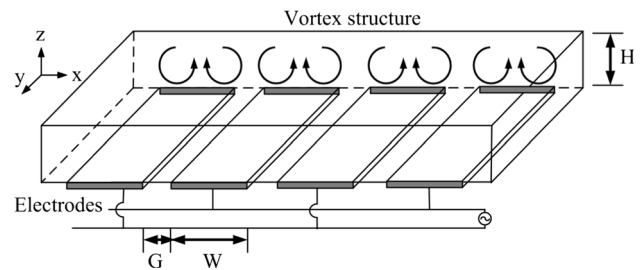

Fig. 1 Schematic diagram of vortex structure in interdigitated symmetric electrodes

the vortex is given via the area integral of the vorticity, $\Gamma = \int_A \omega_y dA$, where the area A is determined via eigenvalues of the strain-rate tensor (λ_2-method) (Jeong and Hussain 1995; Vollmers 2001). The coordinates of the vortex center are given by

$$x_c = \frac{1}{\Gamma} \int_A \omega_y x dA, \; z_c = \frac{1}{\Gamma} \int_A \omega_y z dA. \qquad (2)$$

3 Experimental methods

3.1 Microfluidic device

A micro-device with a straight rectangular micro-channel was used in the present study, shown schematically in Fig. 2. On the substrate of the channel are 7 symmetric Indium Tin Oxide (ITO) electrodes, with a thickness of 120 nm. The width of each electrode is 56 μm and the gap between the electrodes is 14 μm, which leads to the horizontal extent $L = 70$ μm. The electrodes are perpendicular to the axial direction of the channel. The length, width, and height of the channel are about 26 mm, 1 mm, and 48 μm, respectively.

3.2 Fabrication process

The microfluidic device was made by bonding the electrode-deposited glass substrate and the polycarbonate film with a double-sided adhesive acrylic type sheet, as schematically shown in Fig. 2a. The electrodes on the glass substrate were fabricated by a photolithography technique; this procedure is as follows. First, a *Pyrex* wafer with the ITO layer (Praezisions Glas & Optik GmbH, Germany), with a thickness of 0.7 mm, was cut into a size of length × width = 34 mm × 30 mm. The ITO glass plate was spin-coated with a layer of a positive photoresist (HPR HPR504, FUJIFILM, Japan) at 3,000 rpm for 30 s (WS-400 lite series, Laurell Technologies Corp, USA). After the pre-baked treatment at 100 °C for 2.5 min, the mask with the designed pattern was aligned on the glass plate with a hard-contact method. The
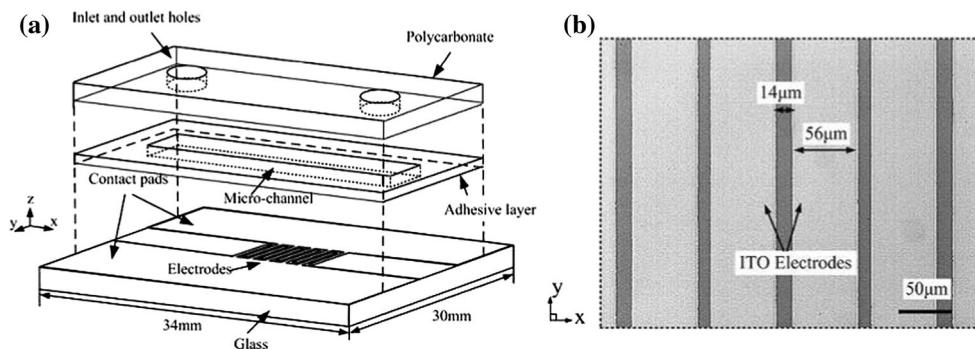
masked glass plate was exposed under the UV light at an energy intensity of 11.4 mW/cm^2 for 5 s. The post-baked treatment at 115 °C was applied on the exposed glass plate for 2.5 min. Subsequently, the exposed glass plate was put into the developer solution (PSLI:H$_2$O 1:1, FUJIFILM, Japan) for 1.5 min, where the exposed photoresist was dissolved. The ITO layer with desired pattern was etched in an etching solution (HCl:H$_2$O:HNO$_3$ = 4:2:1 by volume) for 3 min and then rinsed with DI water several times and blown dry with N$_2$. The electric resistance between two individual electrodes was measured (Multimeter 111, FLUKE, USA). If the electric resistance was not infinity (the measured value is less than 6 MΩ), the procedure of ITO etching would be repeated until the electric resistance was measured to be infinity, >6 MΩ. Finally, the glass plane with desired electrode pattern was put in acetone to remove the photoresist.

Once the electrodes were fabricated, the micro-channel was made in a double-sided adhesive acrylic type sheet with a thickness of 50 μm (8212, 3M^{TM} Optically Clear Adhesive, USA). An Excimer-laser (MICROMASTER, OPTEC Co., Belgium) was used to ablate the outline of the micro-channel. The polycarbonate film (Lexan@4B0217, SABIC Innovative Plastics, Saudi Arabia) was used as the top layer of the channel, with a thickness of 0.5 mm. In this layer, the inlet and outlet holes with a diameter of 1 mm were drilled to load the electrolyte. Finally, the three layers in order (the glass plate with ITO pattern, the double-sided adhesive sheet, and the polycarbonate film) were manually aligned and subsequently bonded together (see Fig. 2).

A chip holder was used to mount the micro-device on the experimental setup, connecting the fluidic tubes and electric wires to the micro-device. In order to completely seal the connection from the chip holder to the inlet and outlet holes of the chip, a rubber O-ring was used and stressed on the chip by the holder. To estimate the thickness of the compressed adhesive sheet, the relative z-position of the particles stuck, respectively, at the top and bottom of the channel was measured by the technique described in Sect. 3.4 The height of the channel is measured to be about 48 μm.

3.3 Experimental setup and procedure

A function generator (Sefram4422, Sefram, the Netherlands) provides an AC signal to the electrode arrays through the contact pads of the device (see Fig. 2). The voltage and frequency applied on the electrodes were measured using a digital oscilloscope (TDS210, Tektronix, USA). The potassium hydroxide (KOH) solution (Sigma-Aldrich Co., USA) was prepared as electrolyte, with a concentration of 0.1 mM. Fluorescent polymer micro-particles with a diameter of $d_p = 2$ μm and a density of 1.05 g/cm^3 (Fluoro-Max, Duke Scientific Corp., Canada) were employed as tracer particles to measure fluid velocity. Fluorescent micro-particle solution in stock was diluted in the KOH solution with a low concentration of about 0.01 % (w/w). The conductivity of the solution after adding the fluorescent micro-particle solution was measured to be about 1.5 mS/m (Scientific Instruments IQ170).

The velocity measurement is performed using the astigmatism micro-particle tracking velocimetry technique (astigmatism μ-PTV) (Chen and Angarita-Jaimes 2009; Cierpka et al. 2010a). A fluorescence microscope with a 20 × Zeiss objective lens (numerical aperture of 0.4 and focal length of 7.9 mm) was used to observe the tracer particles. To illuminate the fluorescent tracer particles, a Nd:YAG laser generation (ICE450, Quantel, USA) was employed to produce a pulsed monochromatic laser beam with a wavelength of 532 nm and energy of 200 mJ per pulse (the time interval of each laser pulse is 6 ns). In order to prevent the over-illumination of seeding particles (and over-heating in the working solution), a transmission mirror (078–0160, Molenaar optics, the Netherlands) was used, to reduce the laser energy from 200 to 16 mJ. The emitted light of the illuminated fluorescent tracer particles has a wavelength of 612 nm. A CCD camera (12-bit SensiCam qe, PCO, Germany) recorded the particle images, with a resolution of $1,376 \times 1,040$ pixel^2. In front of a CCD camera, a cylindrical lens with a focal length of 150 mm (LJ1629RM-A, Thorlabs, USA) was used. A digital delay generator (DG535, Stanford Research
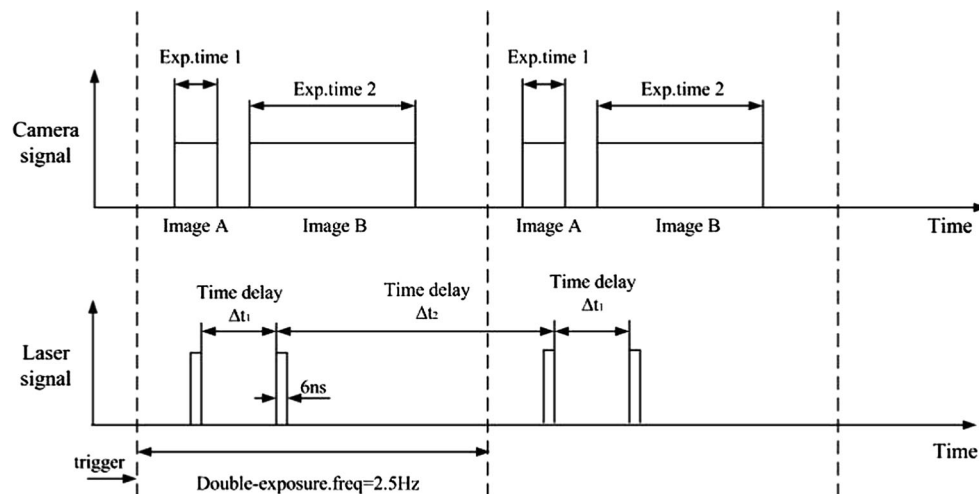
Fig. 3 Schematic of timing sequence of camera signal and laser signal in a digital delay generator. The double-exposure setting of the camera leads to the image recordings in pair, *image A* and *image B*, with a frequency of 2.5 Hz. The time of recording the particle position is determined by the time of triggering the laser pulse in each double exposure. As a result, the timing of the consecutive images has two alternating time delays: the short time delay $\Delta t_1 = 0.03$ s between *image A* and *image B* and the time delay $\Delta t_2 = 0.37$ s between *image B* and *image A* in the next double exposure

Systems, USA) controlled the timing of the laser and camera simultaneously. The image recordings were exported from the camera and imported in the computer.

The double-exposure setting of the camera was chosen, leading to the data acquisition of consecutive frames with two alternating time delays: a short time delay $\Delta t_1 = 0.03$ s and a long time delay $\Delta t_2 = 0.37$ s, as shown in Fig. 3. The short time delay is dictated by the double-exposure setting of the camera, and the long time delay is determined by the time interval of the double exposure, during which the camera's buffer would be written to file. This setting of the camera has an advantage to accurately measure high and low velocities simultaneously.

In the experiment, the electric signal was first switched on. Subsequently, particle imaging was initiated with as little delay as possible. It is important to minimize this delay because the particles progressively tended to collect and become almost "stationary" on the center of the electrodes a short time after the electric signal was applied. The measurement time over a single experimental trial should be short as well, so that there were a sufficient number of "untrapped" particles that still moved freely in the ACEO flow during the measurement. In a single measurement, the total measurement time is 40 s. Correspondingly, 200 consecutive images were recorded at two alternating time delays ($\Delta t_1 = 0.03$ s and $\Delta t_2 = 0.37$ s). Each image contains around 25 particles. To obtain enough data points in one data set, the experiments were repeated using the same parameters for 40 total trials. In all, about 124,000 data points (about 60,000 of them measured in Δt_1 and the others measured in Δt_2) were identified.

3.4 Measurement technique

Due to the anamorphic effect by inserting a cylindrical lens, the astigmatism μ-PTV system has two different magnifications in the two orthogonal orientations, giving rise to a wavefront deformation (elliptical shape) of a fluorescent particle image (Chen and Angarita-Jaimes 2009; Cierpka et al. 2010a). Examining the defocus of the wavefront scattered by a fluorescent particle, one can identify the particle position in the measurement domain and thus establish the three components of the velocity field. Figure 4a depicts a configuration of the astigmatism μ-PTV system used in the present study, where its optical axis is perpendicular against the electrode surface.

A typical image obtained in the experiment is shown in Fig. 4b. It clearly exhibits the elliptical shape of particle images. The particle-image deformation emanates from blurring by the optical system and not by zooming in/out of the camera on a smaller/larger area (The optical blurring is simply a consequence of the working principle and will not result in accuracy loss). Hence, the radius of the ellipse does not correspond to the physical radius of particle, and the camera view in all cases corresponds to the same physical field of view. In order to accurately evaluate the radius of the ellipse in the image-processing procedure, the signal-to-noise ratio (SNR) of image should be as high as possible (Cierpka et al. 2010a). In a preliminary study, it was found that when using tracer particles with a diameter of 2 μm the SNR was high enough that the algorithm gave reliable results. If reducing the diameter of the tracer particle to about 1 μm, the SNR was significantly reduced and

Fig. 4 a Schematic diagram of astigmatism μ-PTV system, where the focal plane is parallel with electrode pattern. **b** Image of fluorescent particles, where the deformation of the particle image is a measure of depth in z-direction
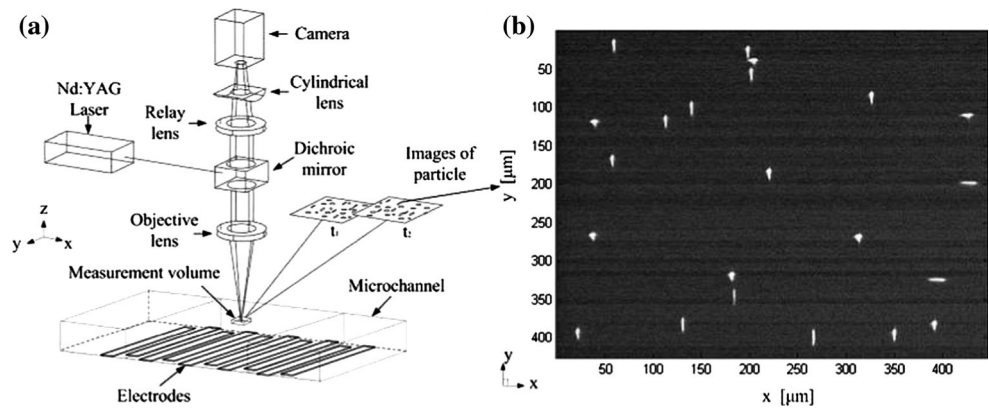
the measurement uncertainty becomes unacceptable. Therefore, in this study, 2-μm tracer particles are used.

3.4.1 Image processing

To estimate the corresponding z-position of the particles, a MatLab program was implemented to process the recorded images, as described below. First, the original images are smoothed by a Gaussian filter with a 11×11 pixel^2 kernel to eliminate spatial fluctuations. By computing a histogram of the image intensity, the most commonly occurring intensity is identified to be the background intensity and subtracted from the smoothed image to reduce background noise. A particle detection algorithm based on the mass intensity in the image (Pelletier et al. 2009) is used to detect the possible image of particles, where each group of contiguous pixels is calculated. To correctly detect the particle, the integrated brightness threshold must be set large enough to lie above the background noise. In this procedure, the primary x- and y-positions of the detected particle center are obtained. Based on the primary positions of the detected particle center, a detection region with 111×81 pixel^2 is chosen from the processed frame to estimate the z-position (the detection region should be set large enough to cover the full image of a single particle). On each detection region, bi-cubic spline interpolation is then applied to improve the resolution of the particle image (Cierpka et al. 2010a). Subsequently, to quantify the image deformation of each particle, the detection region is converted into black and white (B&W) setting according to a gray level threshold (the gray level threshold is based on a histogram of the image intensity in the detection region). Based on the B&W image, the boundary of particle image is identified, and the corresponding diameters of particle images are measured in the x- and y-directions. Based on the calibration functions in the x- and y-directions, the z-position of the detected particle is estimated. Also, the x- and y-positions of the detected particle center are adjusted to be consistent with the detected particle boundary.

Finally, the three coordinates of the particle position are exported.

3.4.2 Calibration

The calibration was done by relating the deformation of the particle image in the x- and y-directions to its relative z-position with respect to two focal planes. The brief procedure of calibration is as follows. One particle, whose position is fixed on the bottom of the channel, is chosen as a reference particle. The channel used was the same as in the experiments and was filled with the same electrolyte. Displacing the bottom plane along the z-axis of the optical system in steps of 2 μm, the diameters of the reference particle image ($d_{n,x}^{\mathrm{ref}}$ [pixel] and $d_{n,y}^{\mathrm{ref}}$ [pixel]) in the x- and y-directions are measured corresponding to the z-positions (z_n^{ref} [μm]), where n is the number of the displacement steps. Then, an eighth-order polynomial fit is applied to relating $d_{n,x}^{\mathrm{ref}}$ and $d_{n,y}^{\mathrm{ref}}$ to z_n^{ref}, as shown in Fig. 5. These fitting functions $d_x^{\mathrm{cal}}(z)$ [pixel] and $d_y^{\mathrm{cal}}(z)$ [pixel] are regarded as intrinsic calibration functions (Cierpka et al. 2010b). The uncertainty of the calibration functions is calculated by using the mean residual between the calibration functions and the measured values

$$\varepsilon_{\mathrm{cal}} = \frac{1}{N} \sum_{n=1}^{N} \sqrt{(d_{n,x} - d_x^{\mathrm{cal}}(z_n^{\mathrm{ref}}))^2 + (d_{n,x} - d_y^{\mathrm{cal}}(z_n^{\mathrm{ref}}))^2},$$

and is about 1.1 pixels.

Once the calibration functions are obtained, the z-position of the particles in the experiment can be determined based on the deviation of the particle diameters between the experimental measurement and the calibration functions as

$$\mathrm{Dev}(z) = \sqrt{(d_x - d_x^{\mathrm{cal}}(z))^2 + (d_y - d_y^{\mathrm{cal}}(z))^2}, \tag{3}$$

where d_x and d_y are the diameters of the particle image measured in the experiment. When $\min(\mathrm{Dev}(z)) < 2\varepsilon_{\mathrm{cal}} \approx 3$ pixels, the particle image is considered to be valid (no
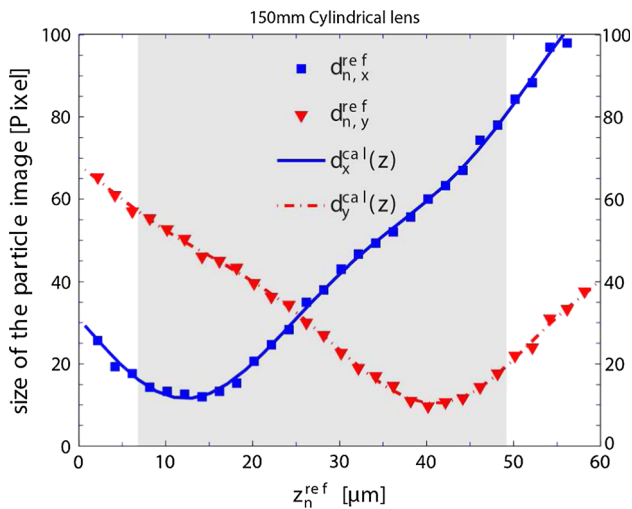
Fig. 5 Size of the deformed particle images ($d_{n,x}^{ref}$ and $d_{n,y}^{ref}$) as function of the reference z-position (z_n^{ref}) and the corresponding calibration fittings ($d_x^{cal}(z)$ and $d_y^{cal}(z)$), where n is the number of the displacement steps. The *highlighted gray* area is the calibration range used in the measurement

overlapping or touching), and the corresponding z is exported as the estimated relative z-position z_{est}.

The accuracy of the estimated relative z-position of the detected particle is limited by the measurable intensity of the particle image (Cierpka et al. 2010a). When it is far away from the two focal planes, the image intensity of the light emitted from the tracer particle is too low to measure. The calibration range is generally chosen based on the distance between the two focal planes due to the high intensity of the particle image (Cierpka et al. 2010b). In this study, the calibration range is set to be about 42 μm (see Fig. 5). Correspondingly, the uncertainty on the estimated z-position according to the reference z-position is calculated as

$$\epsilon_{dev}^z = \frac{1}{N} \sqrt{\sum_{n=1}^{N} (z_n^{ref} - z_{est}(d_{n,x}^{ref}, d_{n,y}^{ref}))^2}, \qquad (4)$$

and is about 0.09 μm.

In the measurements, the water level above a tracer particle depends on the particle's z-position in the channel. Compared to the situation in the calibration, different refractive indices between the water and air lead to an apparent estimated z-position of the tracer particle (z_{est}). This apparent z-position needs to be corrected to the actual z-position z_{act} by

$$z_{act} = z_{est} \cdot (n_{water}/n_{air}), \qquad (5)$$

where $n_{water} = 1.33$ is the refractive index of water and $n_{air} = 1$ the refractive index of air. Correspondingly, the actual depth of the measurable volume is corrected to about 56 μm.

Aberration caused by the optical lens leads to a curvature of the image plane, and therefore when tracer particles

are at the same physical depth, their images vary slightly across the (x, y) plane. If applying a central calibration fitting on a particle that is not in the center of the field of view (FOV), it can give rise to an artificial displacement of the estimated depth of particle (Chen and Angarita-Jaimes 2009; Cierpka et al. 2010b). To compensate for this displacement, a mapping relation for the depth position across the (x, y) plane is introduced. As the optical paths in the (x, z) plane and in the (y, z) plane are different, the corrections in the z-position should be analyzed separately in the x- and y-directions of the (x, y) plane. This results in two field curvatures defined in the (y, z) and (x, z) planes. For simplicity, we assume that the field curvature is cylindrical. Several reference particles, close to the four edges of the FOV, are chosen. The corresponding z-positions are measured. As all the reference particles are in the same plane (at the bottom of the channel), their displacement in the z-position is computed and compared to the one at the center. Based on the artificial displacement of the reference particles, the field curvatures in the (y, z) and (x, z) planes are reconstructed. By combination of the two field curvatures, the absolute offset of particle depth across the (x, y) plane is obtained. After the compensation of z-depth across the (x, y) plane, the standard deviation on z_{est} of the reference particles was less than 0.7 μm.

Since the 3D positions of the tracer particles are known, the particles in consecutive frames are matched by using a nearest-neighbor approach (Crocker and Grier 1996), where possible positions in the next frame are confined to a certain radius from a particle's position in the previous frame. The detection radius of 65 pixels (~ 21 μm) was used in the present study. Correspondingly, the maximum of measurable velocity is about 703 μm/s for Δt_1 and 57 μm/s for Δt_2, respectively. In order to achieve the correct matching by the nearest-neighbor approach, the maximum displacement between the two consecutive positions of a particle should be much lower than the mean distance between particles. As a result, the seeding density of particles is low in the experiment (around 25 particle images were found in each frame).

3.4.3 Error estimation due to uncertainty in position

The measurement uncertainty was estimated by measuring the position of the particle fixed on the channel wall. The maximum residual ε_{max} of the estimated positions in 300 consecutive frames is 1 μm with standard deviation of 0.32 μm in the x-direction, 0.4 μm with standard deviation of 0.25 μm in the y-direction, and 1.1 μm with standard deviation of 0.37 μm in the z-direction, respectively. This uncertainty is attributed to the random error arising from the non-rigidity of the optical system and random fluctuation of image intensity. According to the maximum random

Parameter	Value
Focal length of objective lens	7.9 mm
Numerical aperture	0.4
Magnification of objective lens	20X
Focal length of cylindrical lens	150 mm
Resolution of the CCD	1376×1040 [pixel × pixel]
Magnifications of optical system	$M_x = 3.108$ [pixel/μm]
	$M_y = 2.462$ [pixel/μm]
Field of view	443×422 [μm × μm]
Time delay of image pair	$\Delta t_1 = 0.03$ s
	$\Delta t_2 = 0.37$ s
Diameter of the seeding particle	$d_p = 2 \mu m$
Wavelength of the emitted particle	612 nm
Depth of the measurable volume	56 μm
Uncertainty of position (standard deviation)	$\epsilon_{x.st} = 0.32$ μm
	$\epsilon_{y.st} = 0.25 \mu m$
	$\epsilon_{z.st} = 0.37$ μm

error (the worst situation) on the particle position, the uncertainty on the measured velocity between two consecutive frame was calculated by $e_{vel} = \epsilon_{max}/\Delta t$. It is about 33 μm/s for u_x, 14 μm/s for u_y and 35 μm/s for u_z in Δt_1, and about 2.7 μm/s for u_x, 1.1 μm/s for u_y and 2.9 μm/s for u_z in Δt_2. Note that the uncertainty on the measured velocity becomes weaker with larger time delay Δt due to $e_{vel} \sim \Delta t^{-1}$.

A summary of the experimental details is given in Table 1. Due to the impact of the cylindrical lens, the magnifications in the x- and y-direction are $M_x = 3.108$ [pixel/μm] and $M_y = 2.462$ [pixel/μm], respectively, and the ratio of magnification is $M_x/M_y = 1.262$.

4 Results and discussion

4.1 3D particle trajectories

Figure 6 a depicts the 3D trajectories of tracer particles at a voltage of 2 Volts peak–peak (V_{PP}) and a frequency of 1,000 Hz, where the displacements of the tracer particles were tracked in two alternating time delays: 0.03 and 0.37 s. It reveals that the tracer particles follow the fluid loops. These fluid loops seem primarily periodic over the electrode surfaces. A top view of particle trajectories is given in Fig. 6b for clarity, where the z-component of particle velocity is calculated at each position and indicated in colors. u_z reaches a negative peak when the particles approach the electrode edges, and u_z turns to a positive peak when the particles move from the electrode edge to
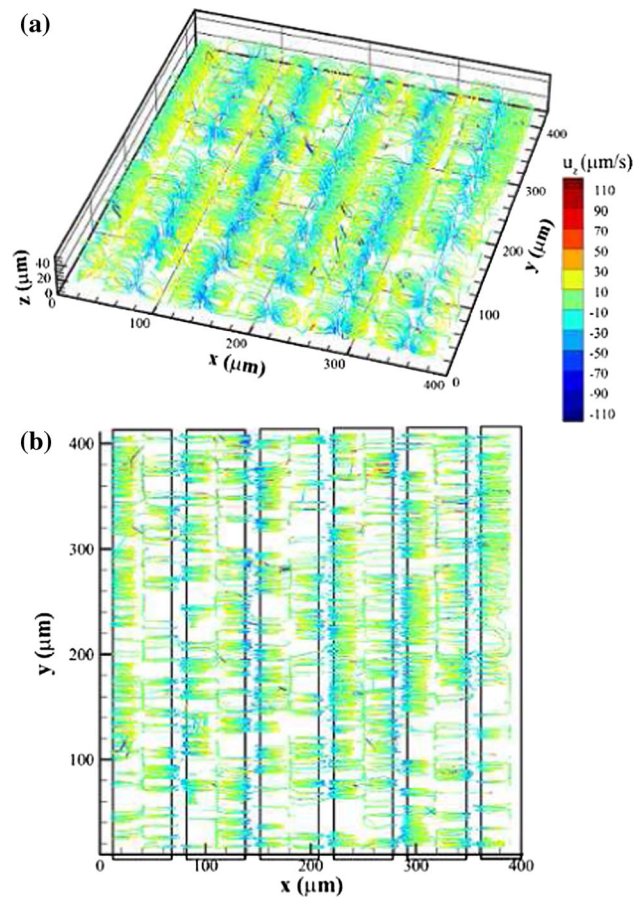

Fig. 6 **a** 3D particle trajectories at applied voltage of 2 V_{PP} and frequency of 1,000 Hz, **b** Top view of the particle trajectories, where the *solid lines* indicate the electrode edges

the center. In Fig. 6a, many of particle trajectories only cover a limited number of consecutive time steps. This is because of the overlapping or touching of particle images which leads to tracking particles that are lost in the next frame. In addition, the aggregation of the particles at the middle of the electrode surface is clearly seen, similar to Green's observation (2002). These particles initially circle in the fluid loops and later several circles get trapped on the center of the electrodes. This phenomenon may be caused by electrokinetic particle–electrode interactions (Nadal et al. 2002; Fagan et al. 2002) or by the local DEP force on the particles close to electrode surfaces (Oh et al. 2009).

The side view of the 3D particle vectors is given in Fig. 7, where the three components of the particle velocity (u_x, u_y and u_z) are represented in colors. In general, the magnitude of $|u_x|$ reaches a maximum, ∼150 μm/s, close to the electrode edge, and falls off rapidly with distance from the edge along the electrode surface and vanishes at the center (see Fig. 7a). When particles approach the center, the magnitude of $|u_z|$ increases significantly and then decreases rapidly with distance in the z-direction (see Fig. 7c). However, a large $|u_z|$ is observed again when

Fig. 7 Particle velocity vectors at 2 V_{PP} and 1,000 Hz and the magnitude of the velocity indicated in *color bars* **a** u_x, **b** u_y and **c** u_z. *Black solid lines* indicate the electrode positions
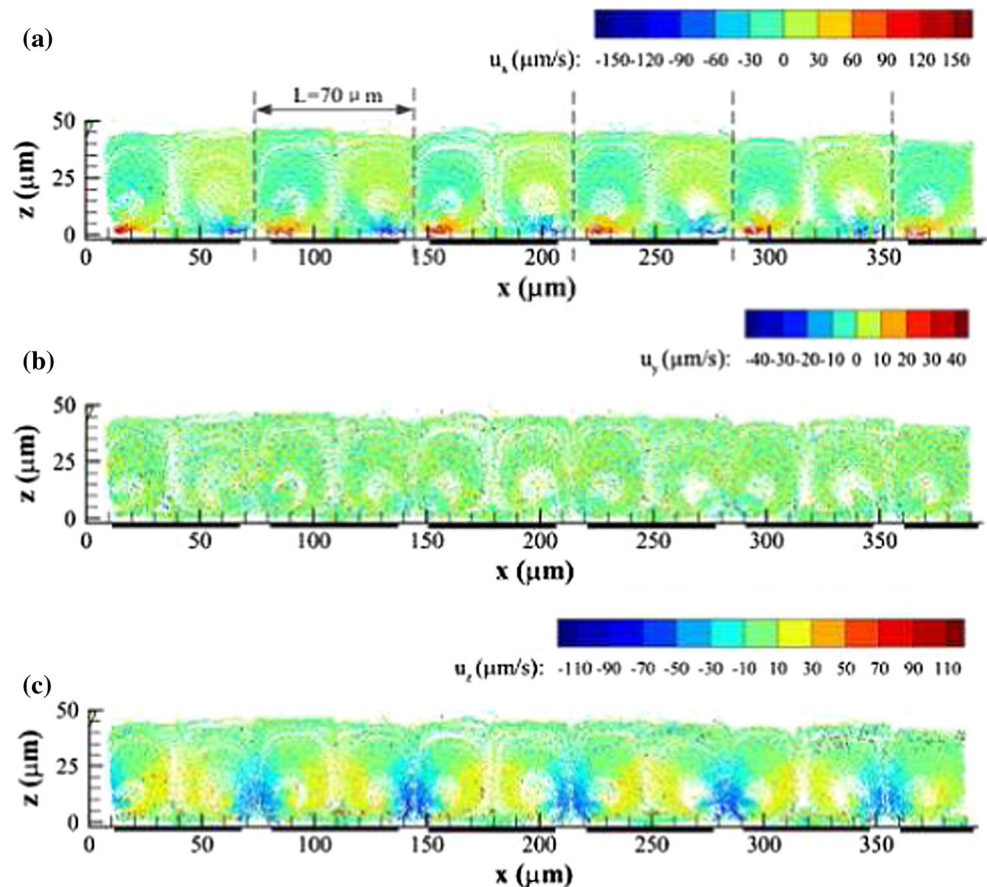
particles move to the gap between the electrodes. Compared to $|u_x|$ and $|u_z|$ varying in a wide range above the electrodes, $|u_y|$ remains small everywhere, varying in the range from -20 to 20 μm/s, as shown in Fig. 7b. According to the magnitude of u_x and u_z in Fig. 7a, c, the periodic structure of the vortical flow is clearly seen, which is consistent with the spatial period of the electrode pattern. The velocity distribution in each spatial period can be seen to be in the same range; the vortex size and shape above each electrode are identical. Since the flow is close to the Stokes limit, the symmetries of boundary conditions and geometry can be adopted, leading to a periodic flow field (Ramos et al. 2003; Speetjens et al. 2011). The present results experimentally demonstrate that using an interdigitated symmetric electrodes generates a periodic ACEO flow field with a periodic distance of L, along the x-axis of the electrode pattern.

4.2 Forces acting on particles

The tracer particles could be under the influence of different forces, including buoyancy, electroosmotic flow, electrothermal flow, dielectrophoresis, Brownian motion, etc (Castellanos et al. 2003). For the tracer particles used in the

experiment, having $d_p = 2$ μm and $\rho_p = 1.05$ g/cm³, the particle velocity due to the buoyancy is $\mathcal{O}(0.1)$ μm/s in the aqueous solution with $\mu = 10^{-3}$ kg/ms and $\rho_f = 1.00$ g/cm³ (Raffel et al. 2007). Compared to the measured ACEO flow (in Fig. 7), which is about $\mathcal{O}(10)$ μm/s, the buoyancy force on the particle is negligible. The Joule heating effect may induce an electrothermal flow with an opposite direction to the measured ACEO flow (Castellanos et al. 2003). Using the analysis in (Ramos et al. 1998), the temperature rise due to the Joule heating is $\triangle T = \sigma V_{rms}^2/k \approx 5 \times 10^{-3}$ K with $V_{rms} = 0.71$ Volts the RMS electric voltage and $k = 0.58$ W/(m·K) the thermal conductivity of the aqueous solution, yielding the electrothermal motion on the order of 10^{-2} μm. Compared to the measured ACEO flow $\mathcal{O}(10)$ μm/s, the electrothermal motion due to the Joule heating can be ignored. Dielectrophoresis (DEP) acts on a polarizable particle due to the non-uniform electric field (Castellanos et al. 2003). We employed the approach used by Kim et al. (2009) to determine the contribution of DEP force on the movement of our polystyrene tracer particle in comparison with the ACEO flow. For the spherical particle, the contribution ratio of DEP force to ACEO flow at the characteristic frequency (ACEO flow is maximum) can be simplified and given as (Kim et al. 2009)

$$\frac{u_{\text{DEP}}}{u_{\text{ACEO}}} = \frac{8\sqrt{k_e}(1+k_e)^2 Re(\chi_{\text{CM}})}{3\pi^2} \frac{d_p^2}{r^2},$$

where u_{DEP} is the particle velocity due to the DEP, u_{ACEO} the fluid velocity induced by AC electroosmosis, $Re(\chi_{\text{CM}})$ the real part of the complex Clausius-Mossotti (CM) factor, k_e the width ratio between the electrodes, r the distance to the center of the gap. The complex CM factor is $\chi_{\text{CM}} = (\tilde{\varepsilon}_p - \tilde{\varepsilon}_m)/(\tilde{\varepsilon}_p + 2\tilde{\varepsilon}_m)$, where $\tilde{\varepsilon}$ is a complex permittivity given by $\tilde{\varepsilon} = \varepsilon - i(\sigma/\omega)$ with $i = \sqrt{-1}$, and the subscripts p and m refer to the particle and suspending medium, respectively (Green and Morgan 1999). Considering the polystyrene particle has $\sigma_p = 10$ mS/m and $\varepsilon_p = 2.55\varepsilon_o$ (ε_o the absolute permittivity of vacuum) (Green and Morgan 1999), in the suspending medium with $\varepsilon_f = 78\varepsilon_o$ and conductivity of $\sigma_f = 1.5$ mS/m, $Re(\chi_{CM})$ is about 0.65 at 1,000 Hz. It suggests the tracer particles experience a positive DEP, which is consistent with experimental observations. As the positive DEP force reaches a maximum at the electrode edges due to the high gradient of the electric current (Green and Morgan 1999), $r = 7$ μm is chosen. For the present electrodes with equal widths, $k_e = 1$. The contribution of DEP can be estimated to be about 6 %, compared to the measured ACEO flow. In this case, the dielectrophoretic force on tracer particles is considered to be small enough to be neglected. This assumption was verified by the experimental observations that most particles were observed to move in the vortex initially, and relative few particles tend to rapidly stick to the electrode edges.

Brownian motion generally causes a random error on the position of the tracer particle suspending in a fluid. Estimating the typical displacement between subsequent images due to Brownian motion, given by $\delta_B = \sqrt{2D\Delta t}$ with $D = k_B T/3\pi\mu\, d_p$ the Stokes-Einstein diffusion coefficient and k_B the Boltzmann constant (Raffel et al. 2007), yields $\delta_B \approx 0.1$ μm and $\delta_B \approx 0.4$ μm for $\Delta t_1 = 0.03$ s and $\Delta t_2 = 0.37$ s, respectively. The corresponding Brownian velocities of the particle, $u_B = \delta_B/\Delta t$, are about 3 and 1 μm/s for Δt_1 and Δt_2, respectively. This velocity is one order of magnitude smaller than the measured ACEO velocity. In this case, the Brownian motion is considered to be negligible. Therefore, under the experimental conditions in the present study, the drag force is dominant for the particle movement and so the particle tracks reliably represent the fluid streamlines of ACEO flow.

4.3 Combined 3D velocity field

Since the flow field above the electrodes is periodic with period L along the x-axis, the velocity field can be studied only in one period, which corresponds to a single electrode.
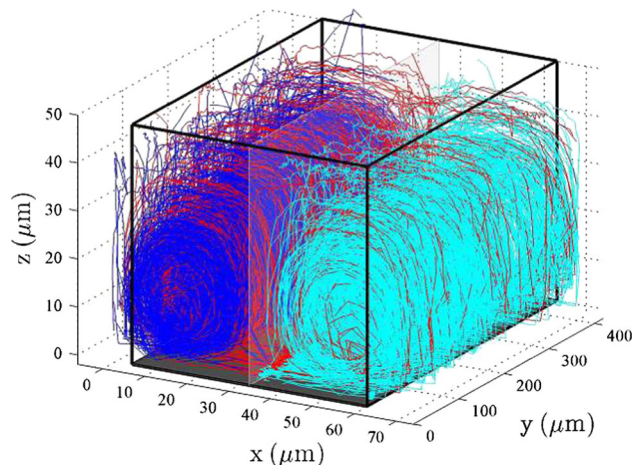

Fig. 8 Combined 3D particle trajectories in the domain with one electrode, where the *blue* and *cyan* indicate trajectories confined to only the left or the right half of the electrode surface. The *red lines* represent the trajectories that cross the symmetry plane. *Black solid lines* outline the combined domain above one electrode surface

The velocity vectors from all electrodes in Fig. 6 were overlaid and combined into a single data set that describes the flow field on an individual electrode. Figure 8 shows the combined 3D trajectories of tracer particles in a flow domain with length L, where blue and cyan colors indicate trajectories sitting either on the left or the right half of the domain with the symmetry plane at the electrode center. It reveals a symmetry of the vortices above the electrode, which is in a good agreement with the numerical prediction on the two-dimension flow field of ACEO vortex (Ramos et al. 2003; Speetjens et al. 2011). Additionally, some trajectories cross the symmetry plane (indicated in red color), implying a symmetry breaking of the vortices. This may be partially due to the small fluctuations of the setup not associated with ACEO flow.

4.4 Error analysis based on particle velocities

Figure 9 depicts the variation of u_x with x at different segments of the combined flow domain (in Fig. 8): at $0 < y < 420$ μm, $z = 3 \pm 0.5$ μm; at $0 < y < 420$ μm, $z = 7 \pm 0.5$ μm; at $0 < y < 420$ μm, $z = 13 \pm 0.5$ μm, and at $0 < y < 420$ μm, $z = 27 \pm 0.5$ μm. As the particle velocities were measured in two time delays Δt_1 and Δt_2, the corresponding velocity points are denoted in two different colors in Fig. 9. As expected, u_x measured in the short time delay Δt_1 varies in a large range compared to the one in Δt_2, since the uncertainty of measurement on the velocity is inversely proportional to the time delay. However, the tendencies of u_x with x in Δt_1 and Δt_2 appear to compare well, indicating that the uncertainty of measurement has no effects to measure the characteristics of ACEO
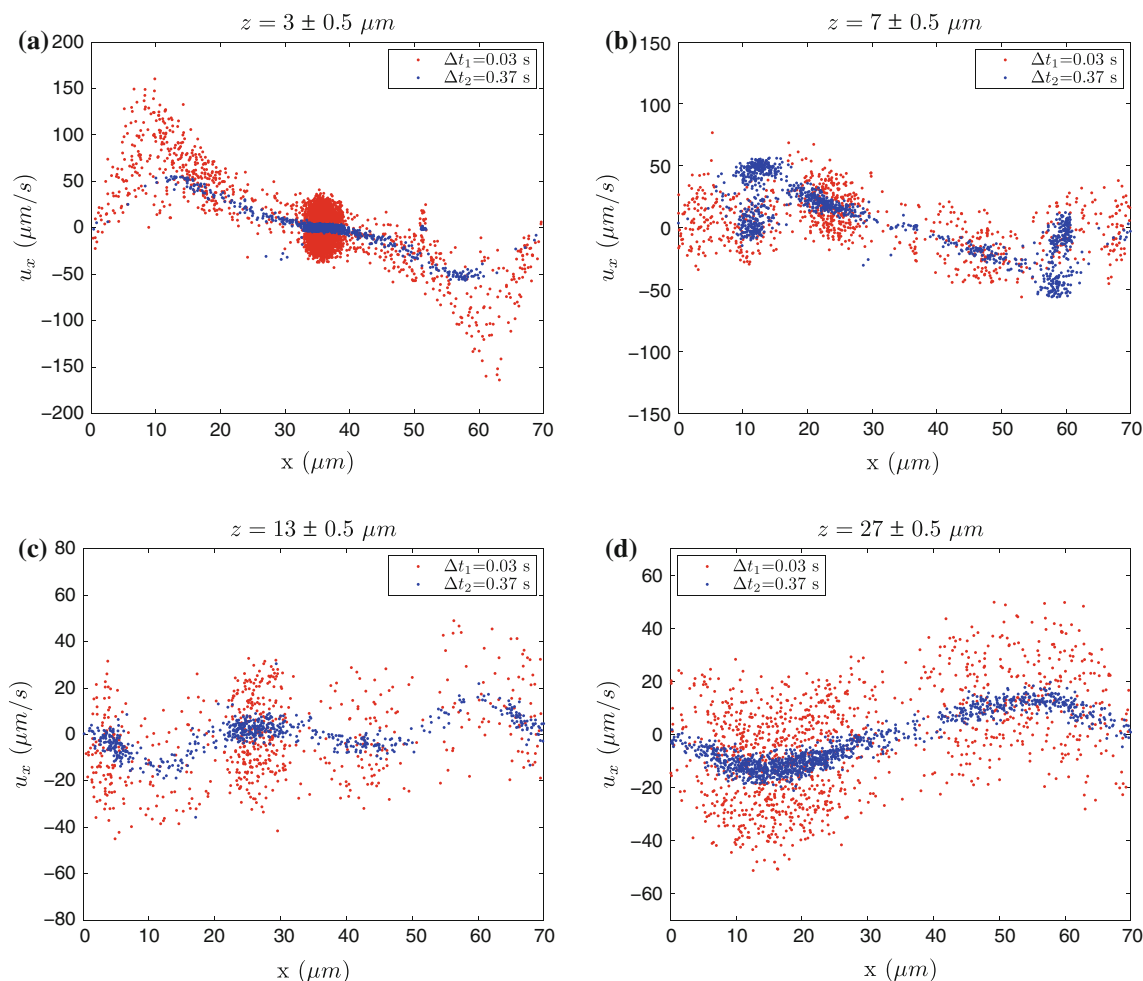
Fig. 9 Scatter plot of the measured x-component particle velocities at $0 < y < 420$ μm, $z = 3 \pm 0.5$ μm (**a**); at $0 < y < 420$ μm, $z = 7 \pm 0.5$ μm (**b**); at $0 < y < 420$ μm, $z = 13 \pm 0.5$ μm (**c**) and at $0 < y < 420$ μm, $z = 27 \pm 0.5$ μm (**d**), where the *blue dots* indicate the data measured at the short time delay $\Delta t_1 = 0.03$ s and the *red dots* represent the ones at the long time delay $\Delta t_2 = 0.37$ s

flow in this study. In addition, due to the limitation of the measurable velocity in Δt_2, Fig. 9a shows that at $z = 3 \pm 0.5$ μm $|u_x|$ measured in Δt_2 is underestimated compared to ones measured in Δt_1. According to $|u_x|$ in Δt_1, the maximum is about 150 μm/s nearby the electrode edges ($x \sim 7$ μm and $x \sim 63$ μm). It can also be observed in Fig. 9a that at $z = 3 \pm 0.5$ μm the variation of u_x in Δt_1 nearby the electrode edges is significantly larger than one above its center. Assuming the uncertainty of measurement is the same, this difference of velocity variation between at the electrode edge and near the electrode center indicates that close to the electrode edge ($z = 3 \pm 0.5$ μm) the gradient of real u_x in the z-direction is larger than one near the center, which is also visible in Fig. 12.

Figure 10 depicts the variation of u_y with x in the cases of Δt_1 and Δt_2 at the same segments as ones in Fig. 9. u_y changes in a small range, from ~ -20 to ~ 20 for Δt_1 and from ~ -2 to ~ 2 μm/s for Δt_2. These variations are very close to the range of the measurement uncertainty on u_y for

Δt_1 (from -14 to 14 μm/s) and for Δt_2 (from -1.1 μm/s to 1.1 μm/s). This indicates that the tracer particles can be considered to be in a quasi-two-dimensional (quasi-2D) flow.

Figure 11 shows the variation of u_z with x in the cases of Δt_1 and Δt_2. In general, the tendencies of u_z with x measured in Δt_1 and Δt_2 are the same. As expected, the variations in u_z for Δt_1 is larger than the one for Δt_2 due to the different measurement error on the velocity. Comparing the measurements on u_x, u_y and u_z in different time delays Δt_1 and Δt_2, it is clear that for single measurement the data points in Δt_2 will give a velocity field with a small variation.

4.5 Quasi-2D flow field

Since the tracer particles can be considered to be in a quasi-2D flow, the raw measured 3D particle velocity vectors are projected in the (x, z) plane, as shown in Fig. 12. As
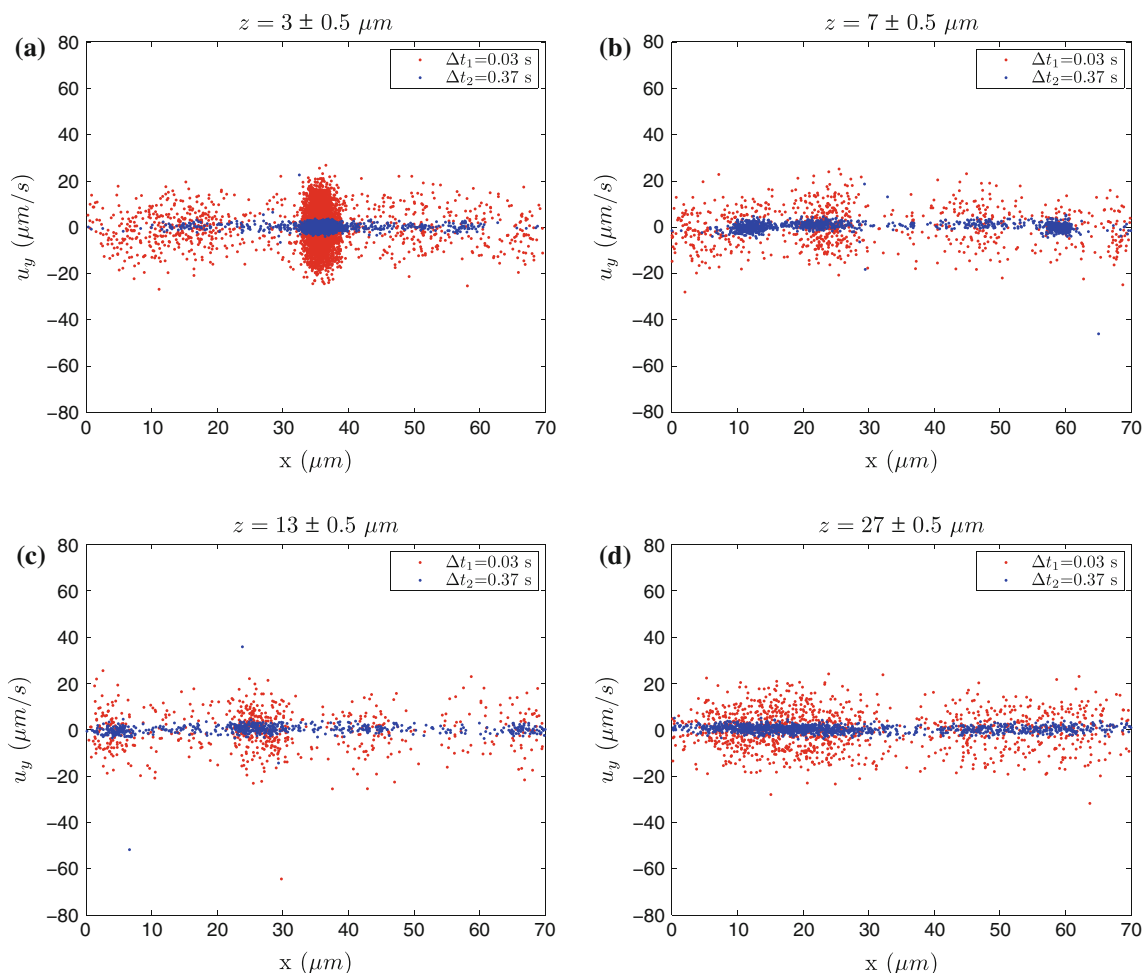
Fig. 10 Scatter plot of the measured *y*-component particle velocities at 0 < y < 420 μm, z = 3 ± 0.5 μm (**a**); at 0 < y < 420 μm, z = 7 ± 0.5 μm (**b**); at 0 < y < 420 μm, z = 13 ± 0.5 μm (**c**) and at 0 < y < 420 μm, z = 27 ± 0.5 μm (**d**), where the *blue dots* indicate the data measured at the short time delay $\Delta t_1 = 0.03$ s and the *red dots* represent the ones at the long time delay $\Delta t_2 = 0.37$ s

expected, two counter-rotated vortices are depicted over the electrode surface. According to the density of the data points, the sticking particles close to the electrode edges and the aggregated particles on the electrode center can be clearly seen. In particular, for the aggregated particles, Fig. 12 reveals that they collect in the range of 1–7 μm away from the electrode surface, rather than being completely stuck on the electrode surface.

Prior to further data analysis, measurement error like sticking particles on the wall should be eliminated. Based on the minimum displacement of the particles close to the wall, a discrimination process is performed: if the *x*-component of displacement of the particle at the distance less than 3 μm away from the wall is less than the maximum measurement error (1 μm) in consecutive frames, this particle is considered to get stuck on the wall in the experiments. It should be noted that in this way most of aggregated particles would be

considered to be the "sticking" particles due to the "stationary" situation and be filtered out as well. As a result, it results in a removal of about 41.2 % of original data measured in Δt_1 and 37.3 % measured in Δt_2.

The obvious outliers in the retained data were then filtered out using a global outlier detection algorithm based on the global standard deviation σ in the entire data (Raffel et al. 2007):

$$\sigma^2 = \frac{1}{N}\sum_{i=1}^{N} e_i^2, \; e_i^2 = \boldsymbol{u}' \cdot \boldsymbol{u}', \; \boldsymbol{u}'(\boldsymbol{x_i}, \boldsymbol{z_i})$$
$$= \boldsymbol{u_{xz}}(\boldsymbol{x_i}, \boldsymbol{z_i}) - \bar{\boldsymbol{u}}_{xz}(\boldsymbol{x_i}, \boldsymbol{z_i}), \tag{6}$$

where x_i and z_i are the coordinates of particle i, $\boldsymbol{u}_{xz} = (\boldsymbol{u_x}, \boldsymbol{u_z})$ the planar velocity field and $\bar{\boldsymbol{u}}_{xz}$ the average of its neighbors. In the present study, $\bar{\boldsymbol{u}}_{xz}$ is calculated using the Gaussian average:
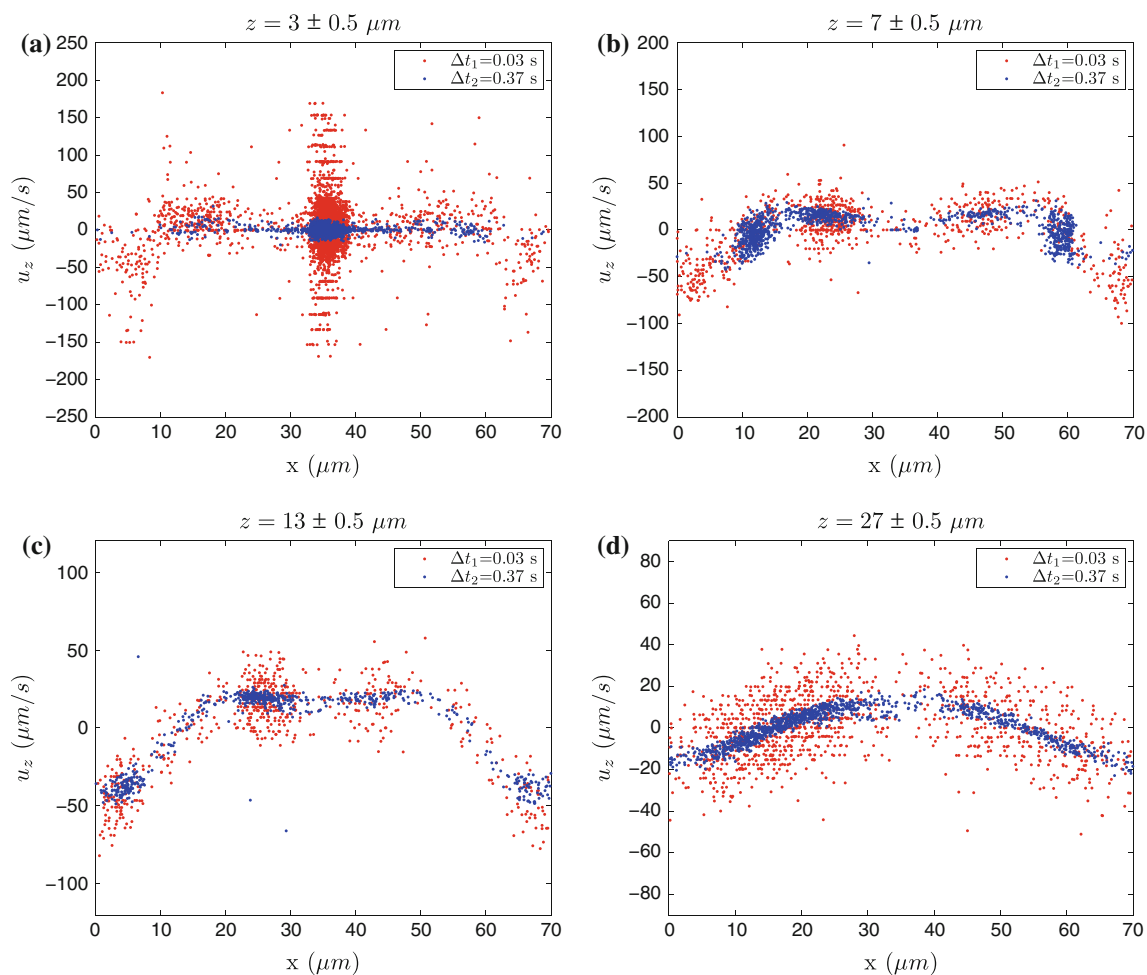
Fig. 11 Scatter plot of the measured z-component particle velocities at $0 < y < 420$ μm, $z = 3 \pm 0.5$ μm (a); at $0 < y < 420$ μm, $z = 7 \pm 0.5$ μm (b); at $0 < y < 420$ μm, $z = 13 \pm 0.5$ μm (c) and at $0 < y < 420$ μm, $z = 27 \pm 0.5$ μm (d), where the *blue dots* indicate the data measured at the short time delay $\Delta t_1 = 0.03$ s and the *red dots* represent the ones at the long time delay $\Delta t_2 = 0.37$ s
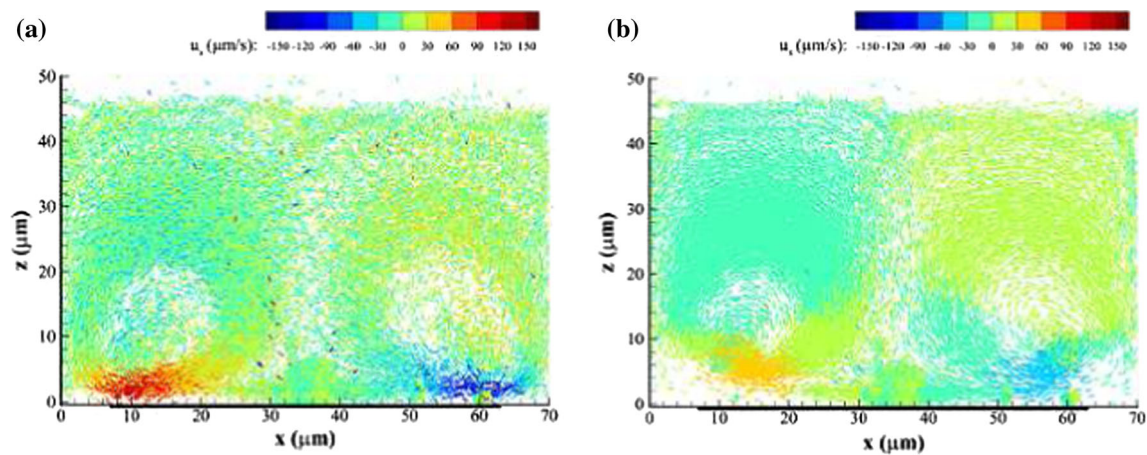

Fig. 12 Quasi-2D particle velocity vectors projected in the (x, z) plane **a** for $\Delta t_1 = 0.03$ s and (b) $\Delta t_2 = 0.37$ s, where u_x is given in *color bars*. *Black solid lines* indicate the electrode positions

$$u_{xz}(x_i, z_i) = \sum_{j=1}^{N} w'_{i,j} u_{xz}(x_j, z_j), \qquad (7)$$

where $w'_{i,j}$ is the normalized weight of the neighboring particles. The weight of the neighboring particle is determined by the relative distance from the neighboring particle j to the particle i:

$$w'_{i,j} = \frac{w_{i,j}}{\sum_{j=1}^{N} w_{i,j}}, \quad w_{i,j} = \exp\left(-\left(\frac{(x_i - x_j)^2}{2\sigma_d^2} + \frac{(z_i - z_j)^2}{2\sigma_d^2}\right)\right) \qquad (8)$$

where x_j and z_j are the coordinates of neighboring particle j, and σ_d the standard deviation of the weight. The standard deviation of the weight σ_d strongly determines the interpolated velocity: a large value results in an over-smoothed velocity field, whereas a small value leads to a less accurate value. Regarding the maximum of random error $\sim 1\ \mu m$, σ_d was set to be 0.5 μm in this study, leading to $\sigma = 33.6\ \mu m/s$ for Δt_1 and $\sigma = 8.1\ \mu m/s$ for Δt_2. The spurious vectors with $e_i > 2\sigma$ are removed from the data set, leading to a removal of 2.2 % (of the retained data after filtering the sticking particle out) for Δt_1 and 6.0 % for Δt_2. In total, 37,000 valid vectors for Δt_1 are taken for the following analysis and 38,000 valid vectors for Δt_2.

The valid vectors were interpolated on a Cartesian grid with the equidistant spacing $\Delta x = \Delta z = 1\ \mu m$. The velocity $\bar{u}_{xz}(x_i, z_i)$ at each point (x_i, z_i) of the Cartesian grid is calculated by using the Gaussian averaging algorithm (according to Eq. 7 and 8). Correspondingly, the standard error of the mean on $\bar{u}_{xz}(x_i, z_i)$ is calculated by

$$SE = \sigma_{local} \Big/ \sqrt{\sum_{j=1}^{N} w_{i,j}}, \quad \sigma_{local}$$
$$= \sqrt{\sum_{j=1}^{N} (u_{xz}(x_j, z_j) - u_{xz}(x_i, z_i))^2 w'_{i,j}} \qquad (9)$$

with j the number of the particles in the region within a radius $2\sigma_d$ from the grid point (x_i, z_i) and N the amount of these particles.

Figure 13 shows the interpolated velocity field in the domain $\Omega : [x, z] = [0, 70] \times [1, 48]$ (μm × μm) for $\Delta t_1 = 0.03\ s$ and $\Delta t_2 = 0.37\ s$, respectively. Both velocity fields illustrate two symmetric counter-rotating vortices above one electrode. For $\Delta t_1 = 0.03\ s$, the highest velocity $\sim 130\ \mu m/s$ is found close to the electrode edges. As expected, this large velocity cannot be found for Δt_2 due to the theoretical maximum measurable velocity less than 57 μm/s. In this case, the data measured in Δt_2 cannot be used to evaluate the velocities close to the electrode edges. According to the results in Δt_1, near the vortex centers the direction and magnitude of the velocity change rapidly (see

Fig. 13a). In contrast, the measurement in Δt_2 fails to capture this rapid change of velocity measured in Δt_1 and instead gives a velocity field with a smoothed change of velocities. Compared to the ones in Δt_1, the position of vortex centers in Δt_2 is located far away against the electrode surface, suggesting that the long time delay cannot be used to measure the velocity of the vortex in the present study. However, compared to in Δt_1, the velocities measured in Δt_2 have a small fluctuation in the region far away from the electrode surface due to the small random error, indicating that the precision of velocity measured in Δt_2 is better in this region.

As the diameter of tracer particles is 2 μm, the particle velocity measured at $z \approx 1\ \mu m$ can be incorrectly measured due to the interaction between the particles and wall, for example, the particles could rebound at the bottom wall due to large $\bar{u}_z$ or roll over the wall surface due to the large variation of $\bar{u}_x$ in the z-direction. Besides, the sticking particles at the wall may locally influence the electric and flow fields. As a result, the following analysis will focus on the velocity field for $z \geq 3\ \mu m$, as shown in Fig. 13.

The velocity profiles of $\bar{u}_x$ as function of x at different z are shown in Fig. 14, where the error bar is indicated in terms of SE. Compared to $\bar{u}_x$ measured in Δt_1, the underestimation of $\bar{u}_x$ in Δt_2 is clearly seen at $z = 3\ \mu m$ close to the electrode edges (in Fig. 14a). When increasing z, the velocity significantly decreases according to the measured velocities in Δt_1. At $z = 7\ \mu m$, the maximum of $\bar{u}_x$ for Δt_1 is less than theoretical maximum measurable velocity (57 μm/s) for Δt_2, and thus, $\bar{u}_x$ in Δt_2 is considered to be reliable. Figure 14b shows that the measured $\bar{u}_x$ for Δt_1 and Δt_2 appears to compare well. With the increase of z into 13 and 27 μm, the measured $\bar{u}_x$ for Δt_1 is very consistent with one for Δt_2, indicating that to measure the low velocities, both methods in Δt_1 and Δt_2 offer the same value. In addition, as expected, $\bar{u}_x$ in Δt_1 has a large fluctuation on the resulting velocities, compared to the ones in Δt_2. The averaged SE on $\bar{u}_x$ is about 5.3 μm/s in Δt_1 and 1.1 μm/s in Δt_2, respectively.

Figure 15 shows the velocity profiles of $\bar{u}_z$ as function of x at different z. At $z = 3\ \mu m$, the maximum of $\bar{u}_z$ measured in Δt_1 is up to about 60 μm/s nearby the center of the gap, as shown in Fig. 14a. In general, the tendencies of $\bar{u}_z$ with x in Δt_1 and Δt_2 appear to compare well at $z = 7, 13, 27\ \mu m$ (Fig. 14b–d). In the measured domain, the averaged SE on $\bar{u}_z$ is 5.2 μm/s in Δt_1 while 1.1 μm/s in Δt_2.

4.6 Vorticity structure

According to the interpolated velocity field $\bar{u}_{xz}$ ($z \geq 3\ \mu m$) measured in Δt_1, the spanwise component of the vorticity was calculated. In the present study, due to the large
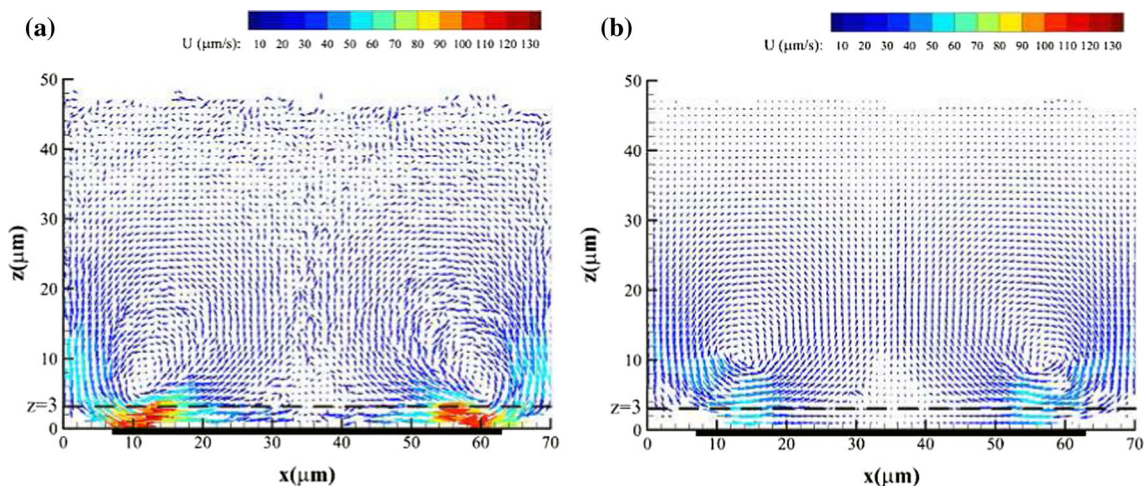
Fig. 13 Quasi-2D velocity field on a regular grid with the spacing $\Delta x = \Delta z = 1$ μm in the (x, z) plane **a** for $\Delta t_1 = 0.03$ s and **b** $\Delta t_2 = 0.37$ s, where the magnitude of the velocity $U = \sqrt{\bar{u}_x^2 + \bar{u}_z^2}$ is given in *color bars*. *Black solid lines* indicate the electrode positions
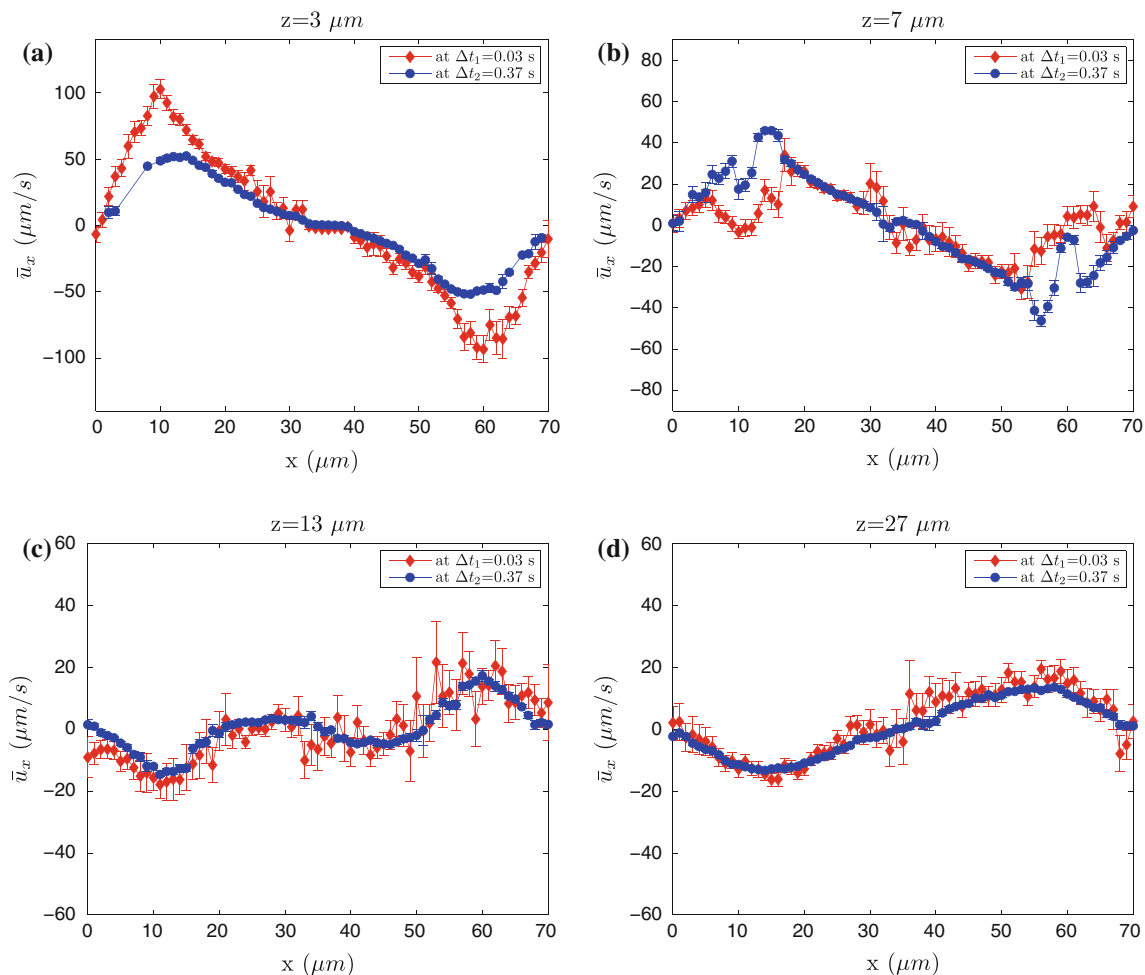

Fig. 14 Profiles of $\bar{u}_x$ against x position at $z = 3, 7, 13, 27$ μm away from the bottom in a quasi-2D velocity field. The *error bars* are given in terms of the standard error of the mean on $\bar{u}_x$

Fig. 15 Profiles of $\bar{u}_z$ against x position at $z = 3, 7, 13, 27$ μm away from the bottom in a quasi-2D velocity field. The error bars are given in terms of the standard error of the mean on $\bar{u}_z$
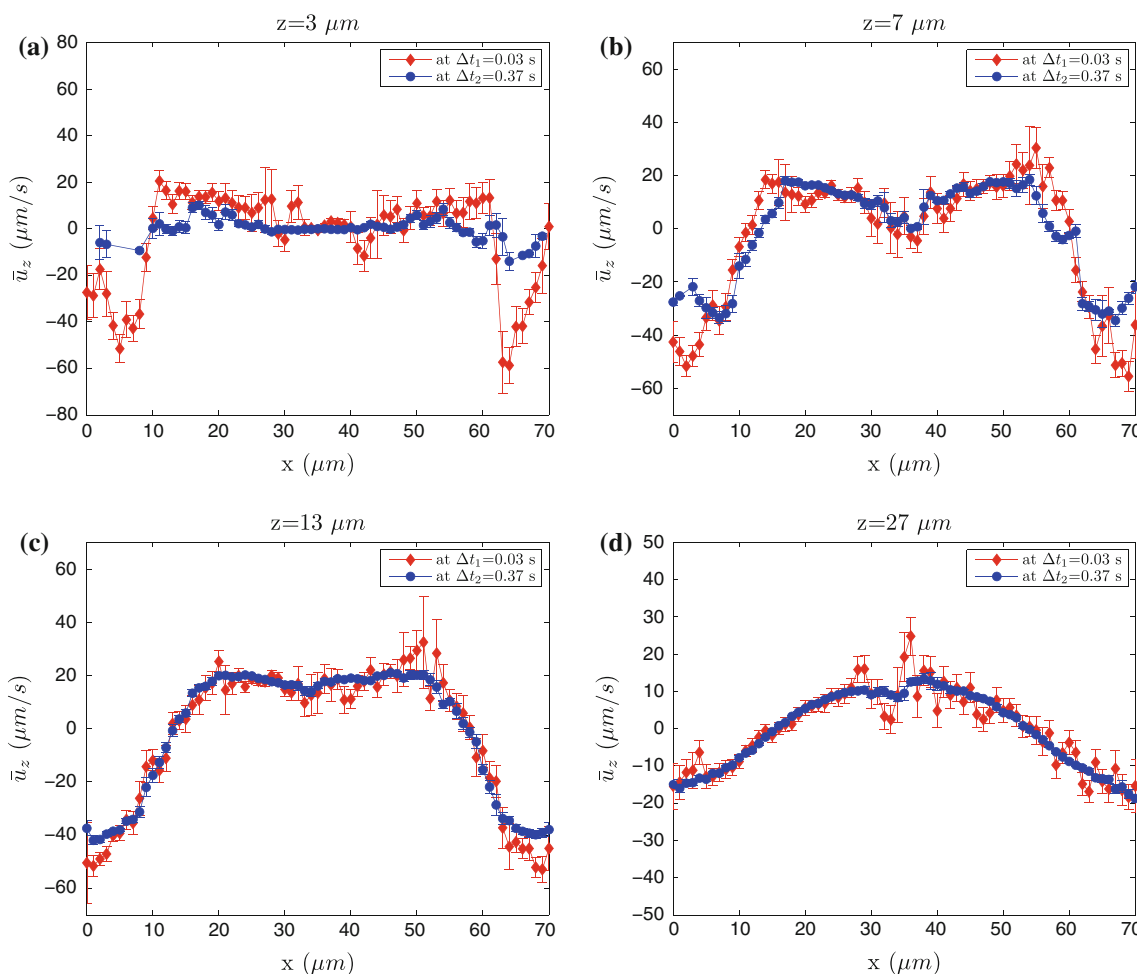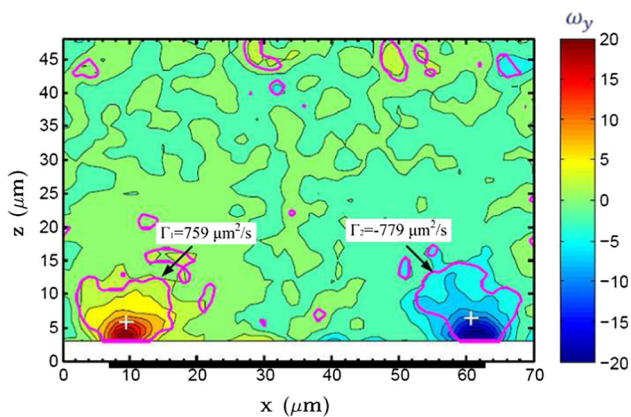

Fig. 16 Vorticity and circulation at 2 V_{pp} and 1000 Hz, where pink solid lines indicate the boundary of the ACEO vortex, $\lambda_2 = -10$. *Black solid line* indicates the electrode position

fluctuation of the measured velocity in Δt_1, the velocity field in Fig. 13a was further smoothed by a combination of discrete cosine transforms and a penalized least-squares approach (Garcia 2011). Figure 16 shows the spanwise vorticity in the domain $\Omega : [x, z] = [0, 70] \times [3, 48]$ (μm × μm). It depicts that both vortices are confined to a small region near the edges of electrode. The vorticity distribution reveals that the vorticity is generated near the electrode edge and dissipated toward the top wall and electrode center. The boundary of the vortex ($\lambda_2 = -10$) exhibits that the vorticity distribution is symmetric. The absolute value of circulation for two vortices is consistent, suggesting that the strength of these vortices due to ACEO on the symmetric electrodes is more or less the same. In addition, the positions of vortex center (referring to Eq. 2) are indicated in Fig. 16, which are at $x_c = 9.7$ μm and $z_c = 6.5$ μm, and at $x_c = 60.7$ μm and $z_c = 7.2$ μm. Correspondingly, the averaged position of vortex center is about 2.5 μm away from the electrode edge and 6.9 μm away from the substrate. It can be noted that the vortex center is different from the position of maximum vorticity, which is due to the elimination of velocity field for $z < 3$ μm.

4.7 Comparison with results in literature

The present experimental observations have some similarities and differences with the results obtained by Green et al. (2000, 2002). Under similar operating conditions, the present velocity distributions above the electrode agree with their observations: the maximum velocity occurs close to the electrode edges and falls off rapidly with distance along the electrode surface. As the measured velocities are low, *i.e.* in the order of 10 μm/s, the ACEO flow to good approximation is a Stokes flow due to the dominance of viscous forces in both our case and that of Green et al. (2000) (*i.e. Re* number ≪1). The streamline patterns and, inherently, the induced vortices therefore are in good agreement as well; the vortical structure in Fig. 13a, e.g., closely resembles the numerical prediction in (Green et al. 2002). However, the width of the electrodes and gaps used in this study is about half that of theirs: 56 and 14 μm, respectively, compared to 100 and 25 μm in (Green et al. 2000, 2002). Hence, despite the close resemblance in vortical structure, the magnitude of the velocity measured in this study is different with theirs. In (Green et al. 2000), the maximum velocity was about 175 μm/s. In the present experiments, a maximum velocity of about 100 μm/s is found, which is considerably smaller (Fig. 14). In theory, a higher velocity is expected in the present study, as the width of electrode and gap is much smaller. This deviation between the experimental observations and the theoretical prediction may be due to different measurement positions. As the ACEO flow is driven by the slip velocity on the electrode surfaces, the magnitude of the velocity considerably decreases with distance to the electrode surfaces. In the present experiments, the velocities are measured at a distance of above 3 μm away from the electrode surfaces. In contrast, in (Green et al. 2000) the velocity measurement was performed within about 1 μm of the surfaces. The measurements depend significantly on the measurement height due to the strong vertical velocity gradients, which may partially explain the difference. In a recent study by Motosuke et al. (2013), a similar flow channel as ours was used, where ITO electrodes were employed, separated by a 25-μm gap. The maximum velocity above the electrodes (measured at about 1 μm away from the surfaces) was about 100 μm/s at 2 V$_{pp}$ and 1 kHz, which is comparable to our results.

5 Conclusions

In this study, the vortical structure due to AC electroosmosis has been experimentally investigated. The 3D particle trajectories above the interdigitated symmetric electrodes were obtained using astigmatism micro-particle tracking velocimetry technique. It reveals that the flow field is periodic over each electrode along the electrode array because of the spatial periodicity of the electrode pattern. This nature of the flow field enables the overlapping of the velocity data points into a single data set that describes the velocity field on an individual electrode. The variations of the particle velocity measured in two time delays ($\Delta t_1 = 0.03$ s and $\Delta t_2 = 0.37$ s) have demonstrated that the 3D velocity field of ACEO flow can be considered as one quasi-2D flow field since the y-component of the particle velocities is small everywhere.

An averaged quasi-2D velocity field on a regular grid in the (x, z) plane was reconstructed based on the different data sets in terms of time delay. The averaged standard error of the mean on the interpolated velocities ($\bar{u}_x$ and $\bar{u}_z$) are about 5.3 and 5.2 μm/s for Δt_1, and 1.1 and 1.1 μm/s for Δt_2. As expected, the measurement with the long time delay has a small measurement uncertainty on the velocity. However, due to the limitation of measurable range of velocity in Δt_2, the velocity data measured in Δt_1 were used to analyze the ACEO flow. The velocity field in Δt_1 has clearly depicted a pair of counter-rotating vortices above the electrode surface; the maximum velocity is close to the electrode edge. Due to the particle–wall interaction, the measured velocities below $z = 3$ μm could be incorrectly measured. Therefore, only the velocity field with $z \geq 3$ μm was taken into account for further analysis. The resulting vorticity has shown that the vortex cores are confined to a region close to the electrode edges. The circulation of each vortex above one electrode has been quantified to be consistent, indicating that both vortices are symmetric as expected. Overall, the vortex flow due to ACEO forcing can be quantitatively evaluated using astigmatism μ-PTV.

References

Bazant MZ, Ben Y (2006) Theoretical prediction of fast 3D AC electro-osmotic pumps. Lab Chip 6:1455–1461

Brown ABD, Smith CG, Rennie AR (2000) Pumping of water with ac electric fields applied to asymmetric pairs of microelectrodes. Phys Rev E 63:016305

Castellanos A, Ramos A, Gonzalez A, Green NG, Morgan H (2003) Electrohydrodynamics and dielectrophoresis in microsystems: scaling laws. J Phys D 36:2584–2597

Chen S, Angarita-Jaimes N et al. (2009). Wavefront sensing for three-component three-dimensional flow velocimetry in microfluidics. Exp Fluids 47:849–863

Cierpka C, Segura R, Hain R, Kähler CJ (2010a) A simple single camera 3C3D velocity measurement technique without errors due to depth of correlation and spatial averaging for micro fluidics. Meas Sci Technol 21:045401

Cierpka C, Rossi M, Segura R, Kähler CJ (2010b) On the calibration of astigmatism particle tracking velocimetry for microflows. Meas Sci Technol 22:015401

Cierpka C, Rossi M, Segura R, Mastrangelo F, Kähler CJ (2011) A comparative analysis of the uncertainty of astigmatism μ-PTV, stereoμ-PTV and μ-PIV. Exp Fluids 1:1–11

Crocker J, Grier D (1996) Methods of Digital Video Microscopy for Colloidal Studies. J Colloid Interface Sci 179:298–310

Fagan JA, Sides PJ, Prieve DC (2002) Vertical oscillatory motion of a single colloidal particle adjacent to an electrode in an AC electric field. Langmuir 18(21):7810–7820

Gagnon Z, Chang HC (2005) Aligning fast alternating current electroosmotic flow fields and characteristic frequencies with dielectrophoretic traps to achieve rapid bacteria detection. Electrophoresis 26:3725–3737

Garcia D (2011) A fast all-in-one method for automated post-processing of PIV data. Exp Fluids 50:1247–1259

Garacia-Sanchez P, Ramos A, Green NG, Morgan H (2006) Experiments on AC electrokinetic pumping of liquids using arrays of microelectrodes. IEEE Trans Dielectr Electr Insul 13:670–677

Green NG, Morgan H (1999) Dielectrophoresis of submicrometer latex spheres. 1. Experimental results. J Phys Chem B 103(1):41–50

Green NG, Ramos A, Gonzalez A, Morgan H, Castellanos A (2000) Fluid flow induced by nonuniform ac electric fields in electrolytes on microelectrodes. I. Experimental measurements. Phys Rev E 61:40114018

Green NG, Ramos A, Gonzalez A, Morgan H, Castellanos A (2002) Fluid flow induced by nonuniform ac electric fields in electrolytes on microelectrodes. III. Observation of streamlines and numerical simulation. Phys Rev E 66:026305

Huang S-H, Wang S-K, Khoo HS, Tseng F-G (2007) AC electroosmotic generated in-plane microvortices for stationary or continuous fluid mixing. Sens Actuators B 125:326–336

Jeong J, Hussain F (1995) On the identification of a vortex. J Fluid Mech 285:69–94

Kim BJ, Yoon SY, Lee KH, Sung HJ (2009) Development of a microfluidic device for simultaneous mixing and pumping. Exp Fluids 46:85–95

Kumar A, Cierpka C, Williams SJ, Kähler CJ, Wereley ST (2010) 3D3C velocimetry measurements of an electrothermal microvortex using wavefront deformation PTV and a single camera. Microfluid Nanofluid 10:355–365

Motosuke M, Yamasaki K, Ishida A, Toki H, Honami S (2013) Improved particle concentration by cascade AC electroosmotic flow. Microfluid Nanofluid 14:1021–1030

Nadal F, Argoul F, Hanusse P, Pouligny B, Ajdari A (2002) Electrically induced interactions between colloidal particles in the vicinity of a conducting plane. Phys Rev E 65:061409

Oh J, Hart R, Capurro J, Noh H (2009) Comprehensive analysis of particle motion under non-uniform AC electric fields in a microchannel. Lab Chip 9:62–78

Park S, Beskok A (2008) Alternating current electrokinetic motion of colloidal particles on interdigitated microelectrodes. Anal Chem 80:2832–2841

Pelletier V, Gal N, Fournier P, Kilfoil ML (2009) Microrheology of microtubule solutions and actin-microtubule composite networks. Phys Rev Lett 102:188303

Raffel M, Willert C, Wereley S, Kompenhans J (2007) Particle image velocimetry: a practical guide. Springer, Germany

Ramos A, Morgan H, Green NG, Castellanos A (1999) AC electric field-induced fluid flow in microelectrodes. J Colloid Interf Sci 217:420–422

Ramos A, Morgan H, Green NG, Castellanos A (1998) AC electrokinetics: a review of forces in microelectrode structures. J Phys D Apply Phys 31:2338–2353

Ramos A, Gonzalez A, Castellanos A, Green NG, Morgan H (2003) Pumping of liquid with ac voltage applied to asymmetric pairs of microelectrodes. Phys Rev E 67:056302

Sasaki N, Kitamori T, Kim HB (2006) AC electroosmotic micromixer for chemical processing in a micro channel. Lab Chip 6:550–554

Speetjens MFM, Wispelaeere HNL, van Steenhoven AA (2011) Multi-functional Lagrangian flow structures in three-dimensional ac electro-osmotic micro-flows. Fluid Dyn Res 43:035503

Studer V, Pepin A, Chen Y, Ajdari A (2004) An integrated AC electrokinetic pump in a microfluidic loop for fast and tunable flow control. Analyst 129:944–949

Vollmers H (2001) Detection of vortices and quantitative evaluation of their main parameters from experimental velocity data. Meas Sci Technol 12:1199–1207

Wu J, Ben Y, Battigelli D, Chang HC (2005) Long-range AC electroosmotic trapping and detection of bioparticles. Ind Eng Chem Res 44:2815–2822